

Novel Single/Dual Circularly Polarized Antennas Based on Polarization-Conversion Reflective Metasurfaces

Yufang Wang¹ and Yuehe Ge^{1, 2, *}

Abstract—We propose single/dual circularly-polarized (CP) antennas based on reflective metasurfaces with cross-polarization conversion. By suspending a probe-fed printed bow-tie dipole or a crossed bow-tie dipole above the reflective polarization-conversion metasurface and appropriately tuning the distance between them, a single-CP or a dual-CP antenna is generated. The theoretical design principle on this novel CP antenna structure has been discussed. Simulations and experiments are conducted to validate the design principle. The measured results show that the proposed single-CP antenna has achieved a 3-dB axial ratio (AR) bandwidth of 8.0%, from 12.67 to 13.72 GHz, and a peak gain of 8.03 dBi, while the dual-CP antenna exhibits a dual-CP AR bandwidth of 7.1%, from 13.09 to 14.05 GHz, and peak gains of 8.49 dBi and 7.03 dBi for left-handed circular polarization (LHCP) and right-handed circular polarization (RHCP), respectively. The measured isolation between the two ports of the dual-CP antenna is less than -20 dB. The operating frequency of the proposed antennas can be easily scaled to other frequencies that are applied to some specific wireless applications.

1. INTRODUCTION

With the rapid development of modern wireless communication technology, high-performance antennas with simple structures and low cost are highly required. Circularly polarized (CP) antennas [1–3] can receive electromagnetic waves with arbitrary polarization and hence exhibit robust radiation performance under environmental interferences which is common in wireless communications. They are widely used in wireless systems, such as radar, satellite, radio astronomy, and terrestrial communication. One of the typical CP antennas is microstrip antennas that feature low profile, easy processing, and low cost. The standard methods to generate CP waves in microstrip antennas are the use of a phase-shift feeding network [4–6] and/or special-shape radiation patches [7, 8].

In the past two decades, metamaterials and artificial materials have been studied well due to their distinctive characteristics to manipulate electromagnetic waves and applied to improve the performance of various antennas [9–20]. Recently, metasurfaces, a kind of 2D metamaterials, attract much attention due to their advantages of thin and compact structure, low loss, low cost, and easy fabrication. Based on them, new methods to generate CP waves have been proposed and studied, such as high impedance surfaces [11–13] and reflective or transmissive polarization converter [12–18]. They have been applied to realize the performance enhancements for conventional CP antennas, such as improving the axial ratio (AR) characteristic [19] and gain [20].

Dual-CP antennas are also required for the demand of the polarization diversity in wireless applications. Recently, various dual-CP antennas have been proposed, including dual-CP dielectric resonator antenna [21], dual-CP patch array antenna [22], dual-CP cavity-backed ring-slot antenna [23], and dual-CP substrate integrated waveguide antenna [24]. Metasurfaces are also applied to realize

Received 28 October 2020, Accepted 5 January 2021, Scheduled 22 January 2021

* Corresponding author: Yuehe Ge (yuehe@ieee.org).

¹ College of Information Science and Engineering, Huaqiao University, Xiamen, Fujian Province 361021, China. ² College of Physics and Information Engineering, Fuzhou University, Fuzhou, Fujian Province 350108, China.

dual-CP antennas. In [25, 26], metasurface polarizers are used as superstrates over small antennas to generate dual-CP waves, while in [27], a dual linearly-polarized (LP) monopole antenna is suspended above a metasurface ground to construct a dual-CP antenna.

In this paper, novel CP antennas are proposed based on probe-fed printed dipole antennas [28, 29] and a metasurface ground. The reflective metasurface, which is able to rotate the linear polarization of incident waves by 90° and provide a designated reflection phase, has been used as the ground plane. With a probe-fed planar printed dipole antenna above the ground, wideband CP waves can be obtained. Simulations using commercial software Ansys HFSS and experiments are carried out to validate this design principle.

2. CP RADIATION MECHANISM

Figure 1 depicts the radiation mechanism of the proposed CP antenna, which is composed of a source antenna and a reflective metasurface that acts as a ground plane and also carries out the 90° -polarization rotation for the incoming waves. The distance between the source antenna and reflective metasurface is h . The source antenna generates upward and downward x -polarized electromagnetic (EM) waves, which can be written as

$$\vec{E}_d = \hat{x}E_0e^{-jkz} \quad (1)$$

$$\vec{E}_l = \hat{x}E_0e^{jkz} \quad (2)$$

where \vec{E}_d and \vec{E}_l denote the upward wave and downward wave, respectively. In the two formulas, the same magnitude, E_0 , is considered for both waves. The downward x -polarized EM wave will be fully reflected by the reflective metasurface, and its polarization will be rotated by 90° . Hence, the reflected wave becomes y -polarized. The reflected EM wave will radiate toward the $+z$ axis and can be expressed as

$$\vec{E}_r = \hat{y}E_0e^{-jkz-jk \cdot 2h+j\phi_r}$$

The total radiation field at z -direction above the source antenna can be written as:

$$\begin{aligned} \vec{E} &= \vec{E}_d + \vec{E}_r \\ &= \hat{x}E_0e^{-jkz} + \hat{y}E_0e^{-jkz-jk \cdot 2h+j\phi_r} \\ &= E_0 \left(\hat{x} + \hat{y}e^{-jk \cdot 2h+j\phi_r} \right) e^{-jkz} \end{aligned} \quad (3)$$

where $k = 2\pi/\lambda$ is the wavenumber in free space, and ϕ_r is the reflection phase of the metasurface ground. According to the definition of circular polarization [30], a CP wave is generated when the following conditions are satisfied:

$$|k \cdot 2h - \phi_r| = 90^\circ \quad (4)$$

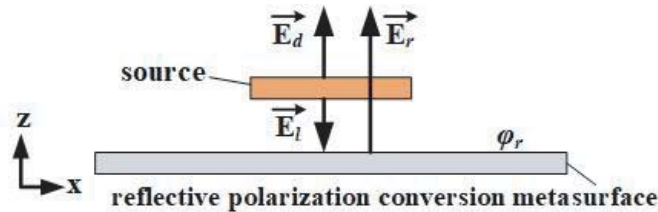


Figure 1. Schematic configuration of the proposed CP antenna.

When Equation (4) is equal to 90° or -90° , a left-handed circularly polarized (LHCP) wave or a right-handed circularly polarized (RHCP) wave is obtained. Therefore, the radiation mechanism of the proposed CP antenna is conceptually explained. According to Equation (4), it is noted that the distance between the source antenna and metasurface and the reflection phase of the metasurface are crucial for achieving and improving the performance of the circular polarization.

3. ANTENNA DESIGN

To realize CP antennas using the above design principle, we apply a printed bow-tie dipole antenna [28] as the source antenna, which is fully planar, has a compact configuration, and is probably able to achieve a higher impedance matching bandwidth and the high isolation between the two crossed bow-tie dipoles [28]. The reflective metasurface is composed of an array of 45°-oriented split rings printed on a substrate and backed by a copper sheet. The split rings can efficiently control the amplitude and phase of the orthogonally-polarized reflection waves and result in a broad operation bandwidth [31]. The structure of the proposed antenna is shown in Figures 2(a) and (b), where a printed bow-tie dipole with a probe excitation is applied. Figures 2(b) and (c) depict the detailed parameters of the printed dipole. A dual-polarized printed bow-tie dipole with two probe excitations is illustrated in Figure 2(d), which can be used to replace the dipole in Figure 2(a) to generate a dual-CP antenna.

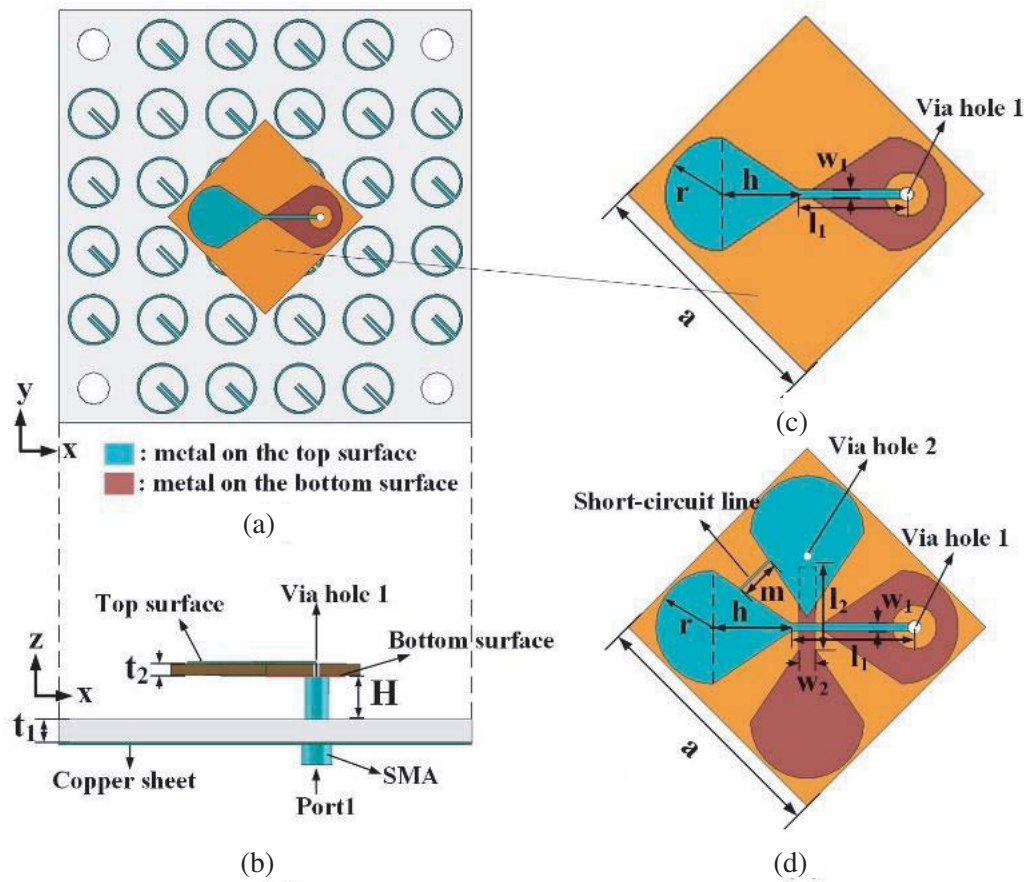


Figure 2. Configuration of the proposed antenna. (a) Top view. (b) Side view. (c) Geometry of the single printed bow-tie dipole antenna. (d) Geometry of the dual-LP printed bow-tie dipole.

3.1. Reflective Metasurface Design

In this paper’s antenna designs, a reflective metasurface is used to fully reflect the LP incoming waves and carry out a 90° polarization rotation. A split ring reflector is applied to implement these functionalities. The unit cell of the metasurface is depicted in Figure 3, which is composed of a single dielectric substrate, a metal ground, and a metal split ring. In this design, an FR4 substrate with a relative permittivity (ϵ_r) of 4.5, loss tangent of 0.02, and thickness of 1 mm is used. The split ring and the ground are printed on the two surfaces of the substrate. The split ring is rotated by an angle of θ so that the 90° polarization

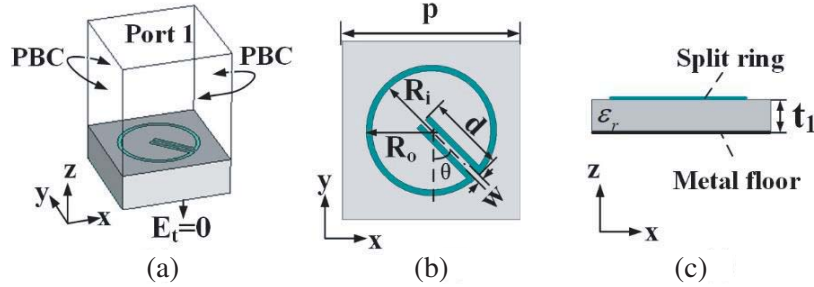


Figure 3. Configuration and simulation model of the proposed unit cell. (a) Simulation model. (b) Top view. (c) Side view.

rotation can be achieved. The characterization of the unit cell was carried out using the commercial software ANSYS HFSS. The simulation model is shown in Figure 3(a) where the periodic boundary conditions are applied to the four sides of the unit cell and the electric boundary condition is applied to the bottom. Figures 3(b) and (c) depict the geometries of the proposed unit cell. The size of the unit cell is $6 \times 6 \times 2 \text{ mm}^3$ (about $0.27\lambda \times 0.27\lambda \times 0.1\lambda$ at 13.5 GHz).

In Equations (1)–(4), an appropriate reflection ϕ_r is required. Therefore, except for carrying out a 90° polarization rotation, the reflective metasurface should provide a designated reflective phase. In the proposed metasurface unit cell, the dimensions of the split ring can be tuned to achieve different reflective phases. Figure 4(a) illustrates the effects on the reflection characteristics at 13.5 GHz when changing the length of parameter d and $R_i = 2 \text{ mm}$, $R_o = 1.8 \text{ mm}$, $w = 0.2 \text{ mm}$. Moreover, the unit cells, which have the same dimension but different rotation angles (45° and -45°), have been characterized, and their performances are also plotted in Figure 4(a). It can be seen that both unit cells can perform 90° polarization rotation and have the same reflection amplitudes, but their reflection phases have a consistent difference of 180° . With the increase of parameter d , the two cells almost provide the required reflection phases within $0\text{--}300^\circ$, while the relative reflection amplitudes are always over 0.89 at 13.5 GHz.

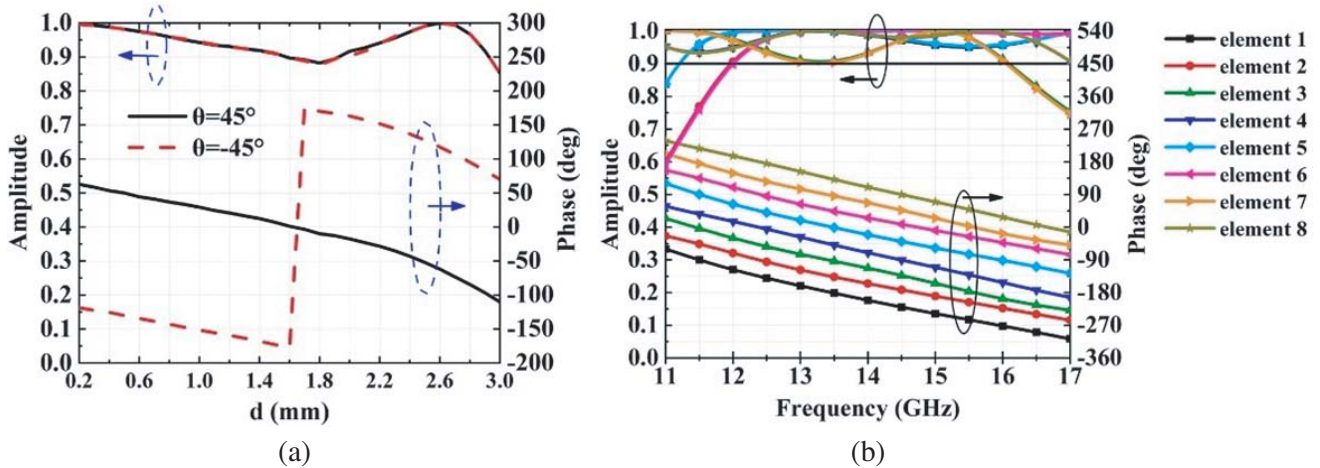


Figure 4. Reflection performance of unit cells. (a) The effects when changing parameter d . (b) Reflection amplitudes and phases for the eight elements in Table 1.

Finally, eight different unit cells are designed. By varying several parameters of the single split ring concurrently, these eight unit cells can provide eight reflection phases with a step of 45° and carry out the 90° polarization rotation with high reflection efficiency in a broad bandwidth. Table 1 lists the parameter values of the eight cells whose characterizations are plotted in Figure 4(b). It is observed that the reflection amplitudes for 90° polarization rotation at 12–16 GHz are more than 0.9, and the reflection phases for every two adjacent elements have a difference about 45° .

Table 1. Parameters of the split-rings for eight different unit cells (unit: mm).

Elements	R_i	R_o	W	d	θ	Elements	R_i	R_o	w	d	θ
1	2	1.8	0.6	2.1	-45°	1	2	1.8	0.6	2.1	45°
2	1.9	1.7	1	2	-45°	2	1.9	1.7	1	2	45°
3	2.2	2	0.2	2.6	45°	3	2.2	2	0.2	2.6	-45°
4	2.2	2	0.9	2.5	45°	4	2.2	2	0.9	2.5	-45°

3.2. Bow-Tie Dipole Elements Design

We first studied a probe-fed linearly-polarized (LP) bow-tie dipole antenna placed above a reflective metasurface, which consists of an FR4 substrate, a 45° -oriented split-ring array, and a metal ground. As shown in Figures 2(a), 2(b), and 2(c), the two arms of the bow-tie dipole are printed on the top and bottom surfaces of a superstrate, respectively. The superstrate uses the F4B substrate, which has a relative permittivity $\epsilon_r = 2.65$, loss tangent $\tan \delta = 0.001$, and thickness of 1 mm. Each arm of the bow-tie dipole is composed of an isosceles triangle and a semicircle. A microstrip stub extending from the dipole arm on the top surface is connected to the inner conductor of the feeding probe through the via hole 1 on the superstrate while its outer conductor is connected to the dipole arm on the bottom surface. The antenna is designed to operate at 13.5 GHz, and the parametric studies are carried out, as shown in Figure 5. It is found that the dimensions of the microstrip stub have outstanding effects on the reflection coefficients. By fixing parameters a , r , and h while only changing parameter l_1 or w_1 , the reflection coefficients are simulated and plotted in Figures 5(a) and 5(b). With the increase of w_1 or l_1 , the impedance matching of the printed dipole varies. The final parameters are: $a = 12$ mm, $r = 2.7$ mm, $h = 4$ mm, $l_1 = 4.6$ mm and $w_1 = 0.4$ mm.

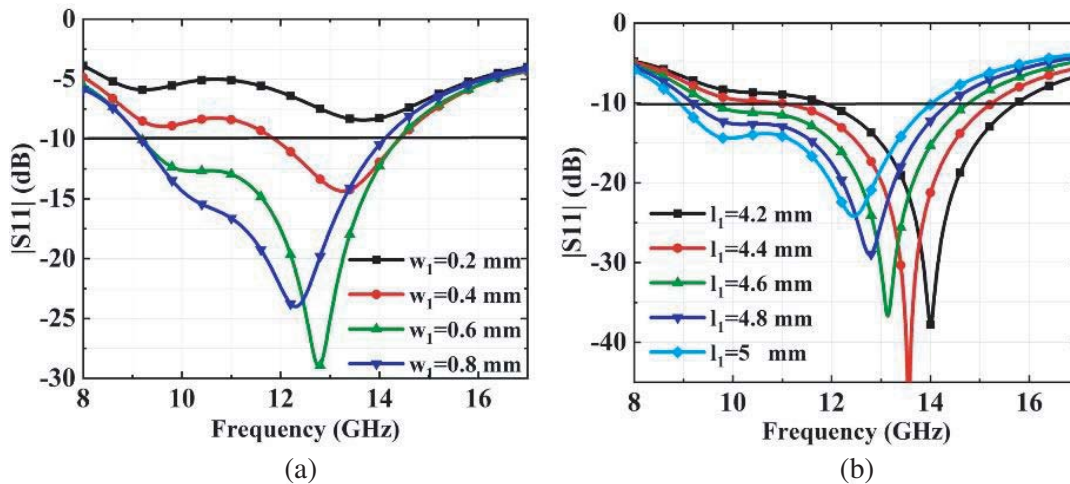


Figure 5. Parametric studies of the impedance matching of the x -polarized bow-tie dipole antenna. (a) Varying w_1 . (b) Varying l_1 .

Based on the above bow-tie dipole antenna, another bow-tie dipole with cross-polarization is added to the same superstrate to form a dual LP bow-tie dipole antenna, whose structure is shown in Figure 2(d). Similarly, another microstrip stub extending from the dipole arm on the bottom surface is connected to the inner conductor of a second feeding probe. Namely, two coaxial probes are applied to feed the x - and y -polarized bow-tie dipoles, respectively. At Port 1, the x -polarized bow-tie dipole is excited, and the feed structure is the same as the bow-tie dipole antenna in Figure 2(c), while the y -polarized bow-tie dipole is excited at Port 2. The inner conductor is connected to the end of the

microstrip stub printed on the bottom surface directly while its outer conductor goes through the via hole 2 and connects the dipole arm printed on the top surface. Without using any wire bridge, this feeding structure makes the dual-polarized antenna planar. In particular, a short-circuit line with a width of 1 mm connecting the adjacent dipole arms of two crossed dipoles printed on the top surface is able to change the current path. This line is the key to improve the isolation of the dual-polarized antenna. Figure 6 plots the comparisons of S parameters between the crossed dipole antennas with and without a short-circuit line. It can be seen that the coupling between two crossed bow-tie dipoles with the short-circuit line is significantly less than that without a short-circuit line, and the -10 dB impedance bandwidth for Port 2 is improved substantially.

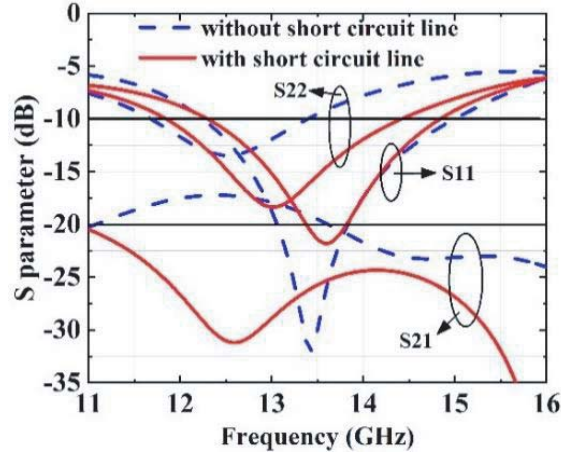


Figure 6. Comparisons of S parameters between the crossed dipole antennas with and without a short-circuit line.

Parametric studies on the dimensions of the two microstrip stubs are also studied, as shown in Figure 7. It is found that increasing the length and shortening the width of the two microstrip stubs can improve the isolation between ports 1 and 2. As mentioned earlier, the microstrip stubs printed on the top and bottom surfaces are used to excite the x -polarized and y -polarized bow-tie dipoles, respectively. Hence, as parameters w_1 and l_1 increase, the resonance for Port 1 ($|S_{11}|$) moves toward lower frequency while they have a minor effect on $|S_{22}|$. Similarly, as parameters w_2 and l_2 increase, the resonance for Port 2 ($|S_{22}|$) moves toward lower frequency, and the bandwidth is enhanced while they have a minor effect on $|S_{11}|$. Finally, the parameters are chosen as follows: $a = 12$ mm, $r = 2.7$ mm, $h = 4$ mm, $l_1 = 5.1$ mm, $w_1 = 0.35$ mm, $l_2 = 3.2$ mm, and $w_2 = 0.8$ mm.

4. PARAMETERS STUDIES ON THE CP PERFORMANCE

To further study the proposed CP antenna, the effects of some important parameters on S parameters, axial ratio (AR), and gain are studied. In each of these studies, only one parameter is changed while others are fixed. According to Equation (4), it is known that the crucial parameters to improve the CP performance are the reflection phase of the reflective metasurface and the distance (H) between the dipole and the reflective metasurface. In the studies below, Element 3 in Table 1 is chosen to form the reflective metasurface.

4.1. The Single-CP Antenna

The single-CP antenna consists of a printed bow-tie dipole antenna and a reflective metasurface formed by 6×6 split-ring elements. Figure 8 shows the effects of the different H . It can be seen that with the increase of the height, the operating frequencies of reflection coefficients and AR move toward lower frequencies, and the impedance matching will deteriorate while the gain is improved. Moreover, the

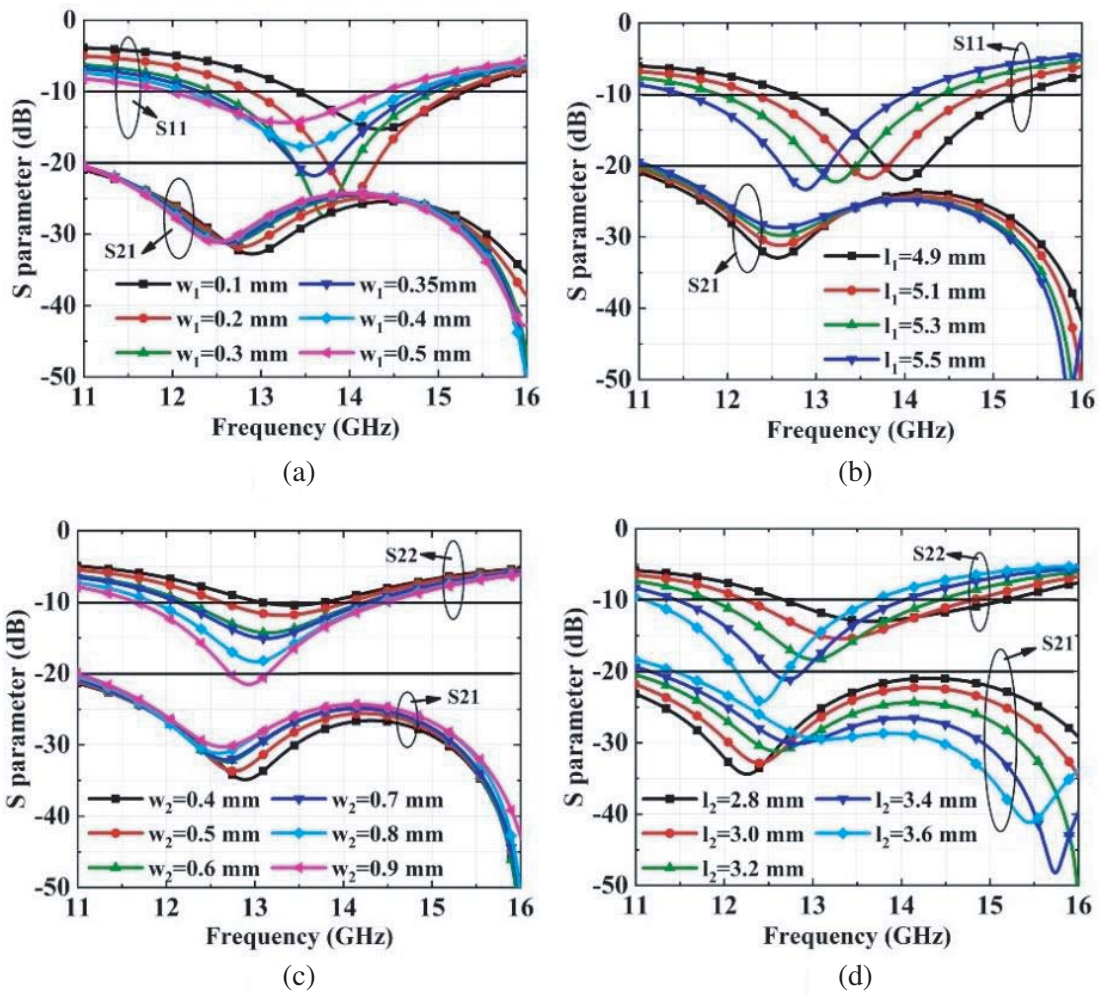


Figure 7. Effects of dimensions of the cross bow-tie dipole antenna on S parameters. (a) Varying w_1 . (b) Varying l_1 . (c) Varying w_2 . (d) Varying l_2 .

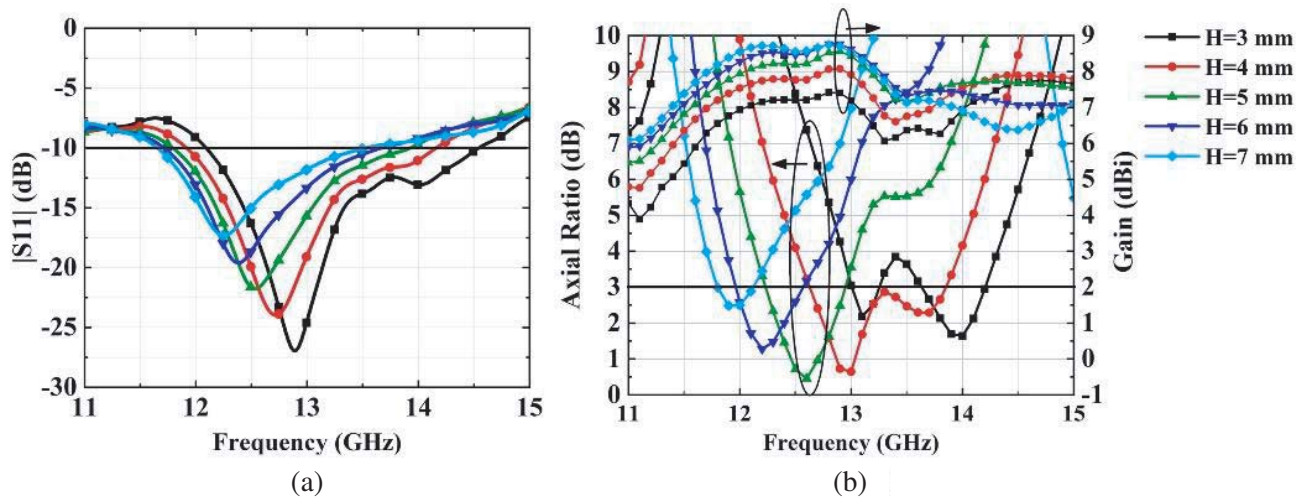


Figure 8. Effects of parameter H on (a) S parameters and (b) ARs and gains.

3-dB AR bandwidth usually falls into that of the -10 -dB $|S_{11}|$. Finally, the optimal AR is obtained when $H = 4$ mm, approximately a quarter wavelength in the operating frequency band.

Figure 9 illustrates the effects of the different d of split rings. When the value of d increases by a step of 0.1 mm, which means that the reflection phase decreases by 10° , the reflection coefficients are improved while the gains are reduced. The optimal d is 2.6 mm for the 3 dB AR bandwidth.

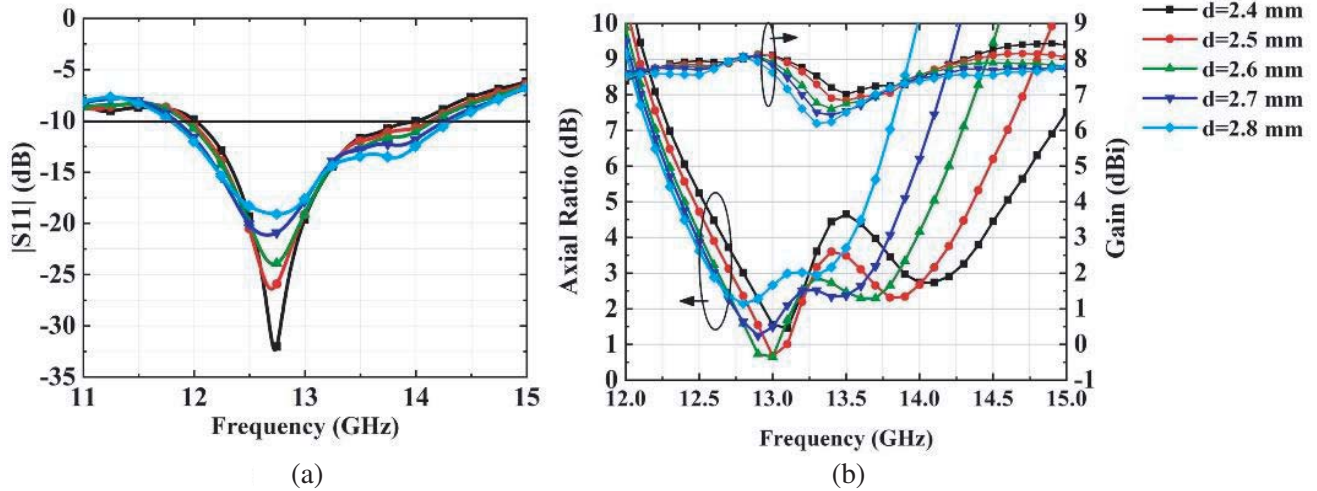


Figure 9. Effects of parameter d on (a) S parameters and (b) ARs and gains.

Figure 10 plots the 3D radiation patterns for the single bow-tie dipole antenna with or without the reflective metasurface ground. It is observed that the gain increases when loading the reflective metasurface, a similar effect to that when loading a metallic ground. The novelty here is that the CP reflective wave is generated.

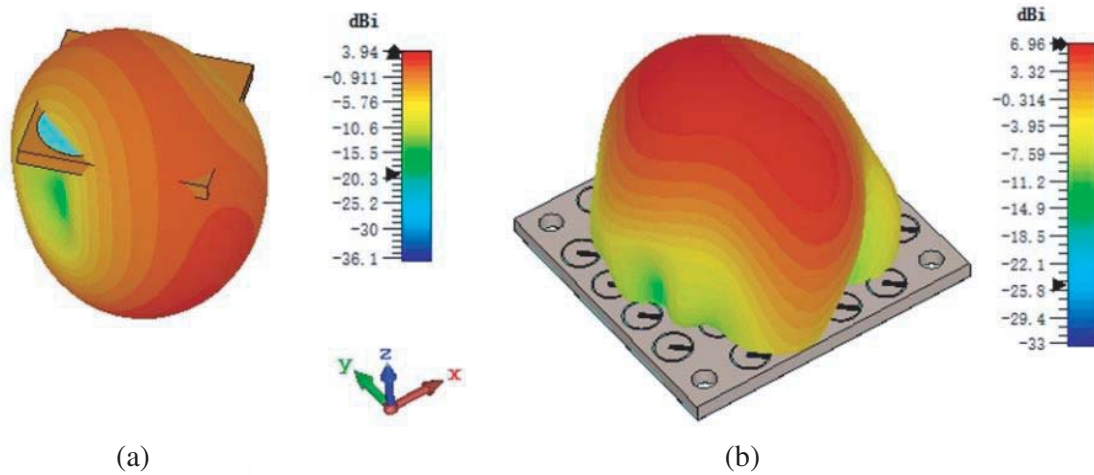


Figure 10. 3D Radiation patterns for the single-CP antenna. (a) The source antenna. (b) The proposed single-CP antenna.

4.2. The Dual-CP Antenna

The dual-CP antenna consists of two printed crossed bow-tie dipole antennas and a reflective metasurface with 4×4 metal split ring elements. The S parameters, ARs, and gains with different H of the dual-CP antenna are also studied, and the results are plotted in Figure 11. As the parameter H increases, when

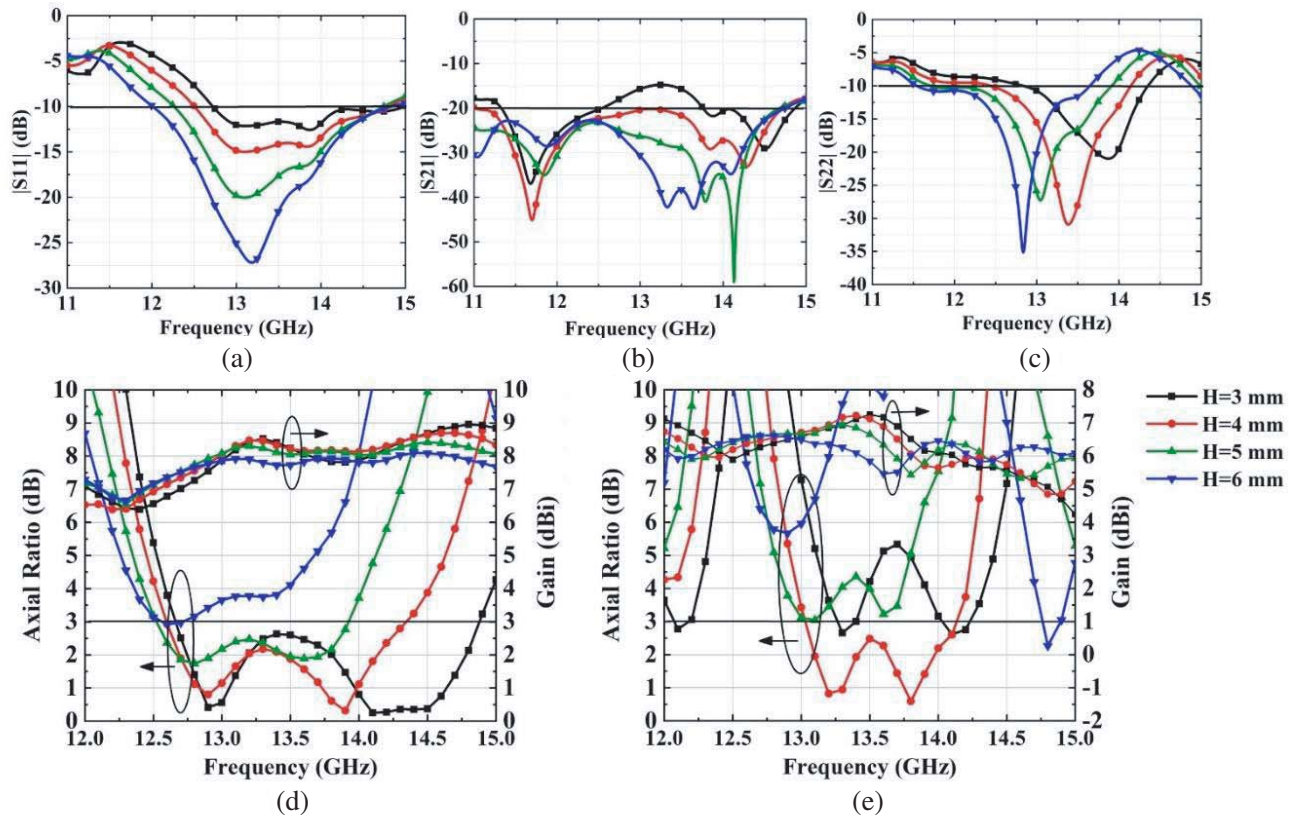


Figure 11. Effects of the parameter H of the dual-CP antenna on (a) S_{11} , (b) S_{21} , (c) S_{22} , (d) ARs and gains when port 1 is excited and (e) ARs and gains when port 2 is excited.

port 1 is excited, the reflection coefficients $|S_{11}|$ become better; the 3-dB AR bandwidth becomes narrow; and the gain decreases. When port 2 is excited, the operating frequency of the reflection coefficient $|S_{22}|$ shifts toward the lower frequency, and the gain decreases. Meanwhile, the isolation between port 1 and port 2 deteriorates with the increase of parameter H . Finally, the optimal H value is 4 mm for both CP modes.

The effects of the different values of parameter d of the split ring are shown in Figure 12. The different d will have little impact on the S parameter. When parameter d increases from 2.4 mm to 2.8 mm, the ARs and gains for ports 1 and 2 have similar trends. The optimal AR for the two CP modes is obtained when $d = 2.57$ mm.

Figure 13 shows the 3D radiation patterns for the crossed bow-tie dipole antenna and dual-CP antenna. Similarly, the gains of both CP modes are higher than those of the crossed dipole antenna. It is observed that the radiation patterns for all of them are less symmetric than those in Figure 10 due to the interaction between the two dipoles.

5. SIMULATION AND MEASURED RESULTS

Based on the above studies, both the proposed single CP antenna and dual-CP antenna were fabricated and measured using a far-field testing system in a microwave anechoic chamber. Figure 14 shows the mounting and measurement setup in the microwave anechoic chamber. The size of the superstrate with the printed dipole antenna is $12 \times 12 \times 1 \text{ mm}^3$ ($0.54\lambda \times 0.54\lambda \times 0.05\lambda$ at 13.5 GHz) while that of the reflective metasurface is $36 \times 36 \times 2 \text{ mm}^3$ ($1.62\lambda \times 1.62\lambda \times 0.09\lambda$ at 13.5 GHz) with 6×6 metal split rings for the single-CP antenna or 4×4 metal split rings for the dual-CP antenna. Several small nylon poles and screws space the superstrate and metasurface and fix them to the rotating platform. Two

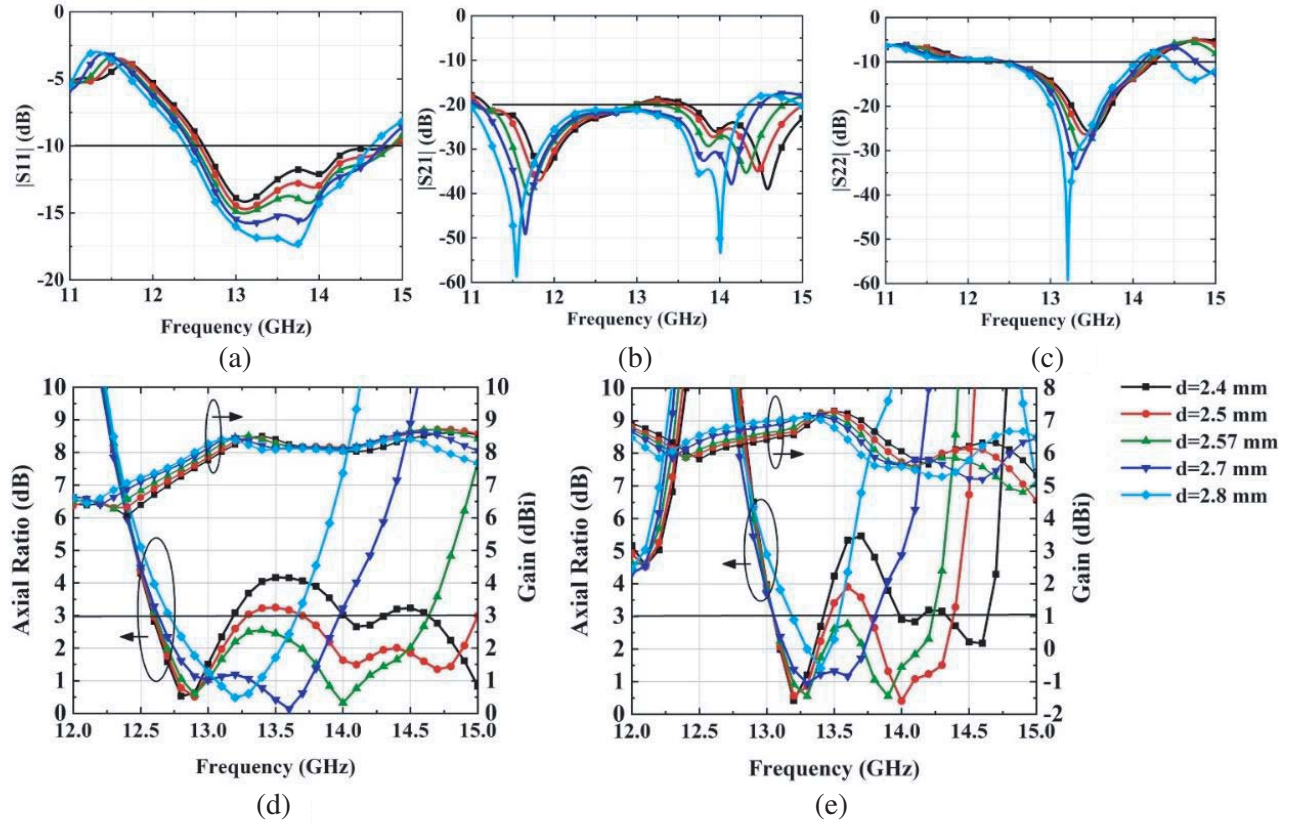


Figure 12. Effects of the parameter d of the split rings on (a) S_{11} , (b) S_{21} , (c) S_{22} , (d) ARs and gains when port 1 is excited and (e) ARs and gains when port 2 is excited.

SMA connectors were applied to the port of the dipole to feed the antenna. The total height of the whole antenna prototypes is 7 mm (0.315λ at 13.5 GHz).

5.1. The Single-CP antenna

Simulated and measured reflection coefficients, ARs, and gains are plotted in Figure 15, which show good agreements. It can be observed that the measured impedance bandwidth for $|S_{11}| < -10$ dB is from 12.06 to 13.92 GHz. The measured 3-dB AR bandwidth is from 12.67 to 13.72 GHz, about 8.0%, which falls into the -10 dB impedance bandwidth. The measured peak gain within the 3-dB AR bandwidth is 8.03 dBi at 13.4 GHz, which is 0.5 dB lower than the simulated one and significantly greater than that of the printed dipole only (less than 4 dBi). Figure 16 depicts the measured radiation patterns at 13.5 GHz. It is noted that an LHCP wave is obtained.

5.2. The Dual-CP Antenna

The simulated and measured results on S parameters, ARs, and gains for the designed dual-CP antenna are given in Figure 17. It can be observed that the measured results reasonably conform to simulated ones. The measured impedance bandwidth for Port 1, determined by $|S| < -10$ dB, is from 12.19 to 14.44 GHz, while for Port 2 it is from 12.87 to 14.33 GHz. The measured isolation between Port 1 and Port 2 remains above 20 dB or $|S_{21}| < -20$ dB over the bandwidth 11 to 14.78 GHz, which covers the entire impedance bandwidth.

As observed in Figure 17(b), when port 1 is excited, the designed antenna operates at the LHCP mode. The simulated 3-dB AR bandwidth is 14.9% (12.61–14.64 GHz) while the measured one is 12.7% (12.67–14.39 GHz). When port 2 is excited, the designed antenna operates at the RHCP mode.

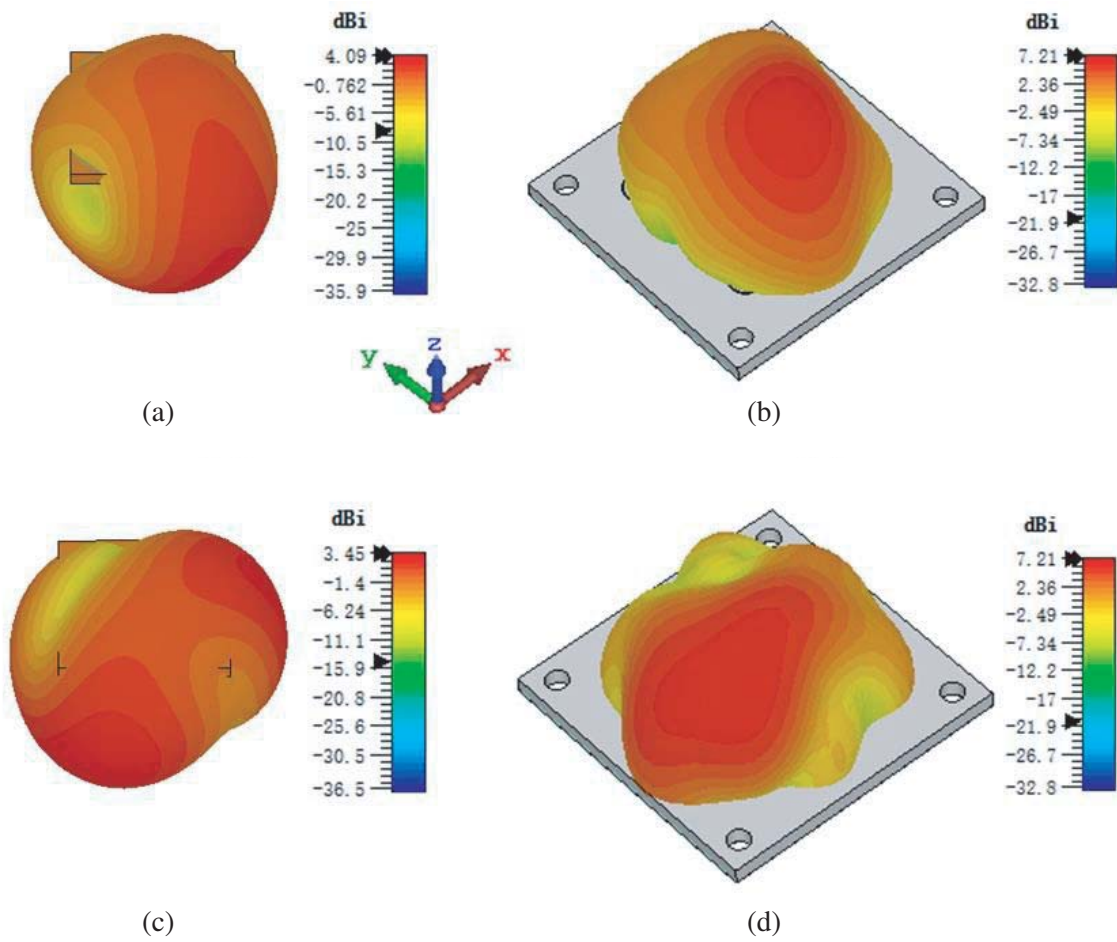


Figure 13. 3D radiation patterns for the dual-CP antenna. (a) The crossed dipole antenna when port 1 is excited. (b) The dual-CP antenna when port 1 is excited. (c) The crossed dipole antenna when port 2 is excited. (d) The dual-CP antenna when port 2 is excited.

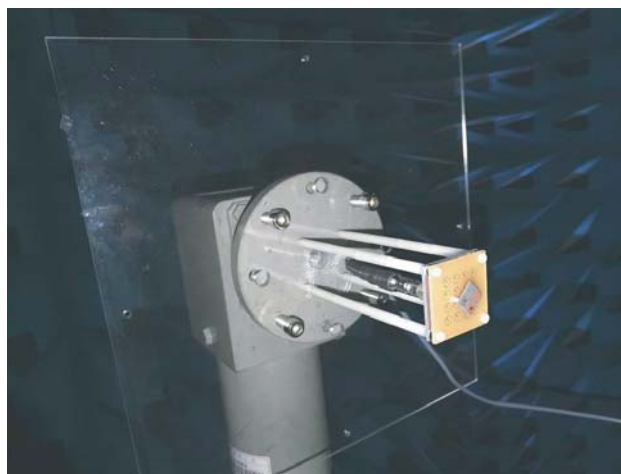


Figure 14. The proposed dual-CP antenna prototype under test.

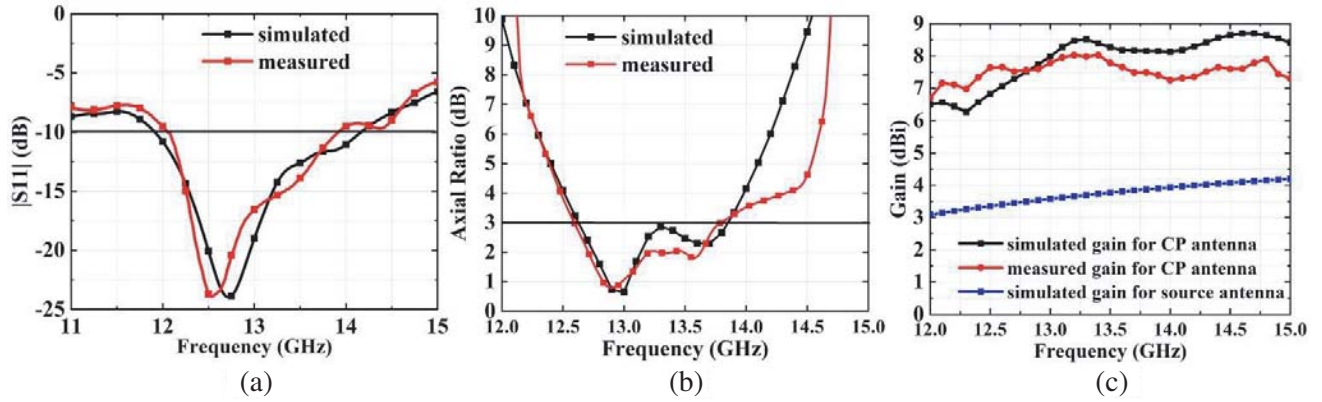


Figure 15. Simulated and measured results for the single-CP antenna. (a) $|S_{11}|$. (b) AR. (c) Gain.

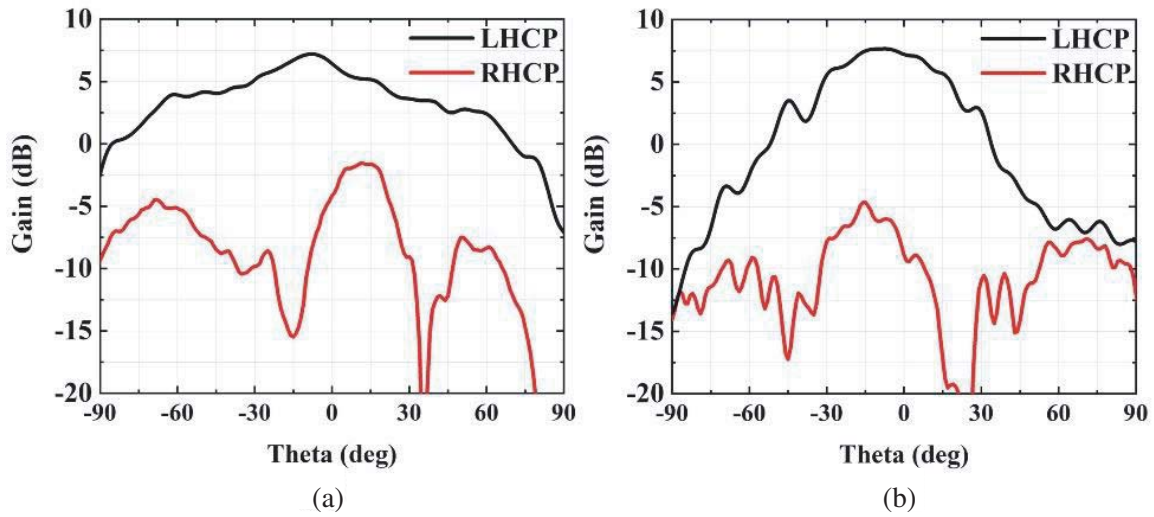


Figure 16. Measured CP radiation patterns at 13.5 GHz for the designed single CP antenna. (a) XOZ plane. (b) YOZ plane.

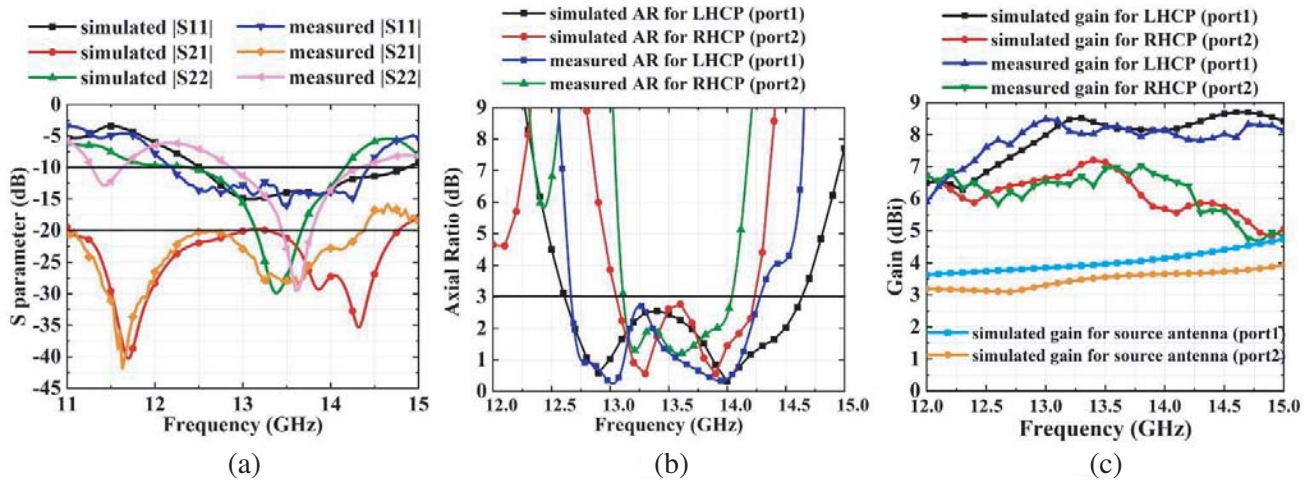


Figure 17. Simulated and measured results for the dual-CP antenna. (a) S parameters. (b) AR. (c) Gain.

The simulated 3-dB AR bandwidth is 8.7% (13.05–14.23 GHz) while the measured one is 7.1% (13.09–14.05 GHz). Comparing the simulated and measured results, the measured AR bandwidths are smaller than the simulated ones. It is observed that the 3-dB AR bandwidths for LHCP and RHCP fall into the impedance matching bandwidths, which are determined by -10 -dB $|S_{11}|$ and $|S_{22}|$, respectively. The measured peak gains for LHCP and RHCP, shown in Figure 15(c), are 8.49 dBi at 13 GHz and 7.03 dBi at 13.8 GHz, respectively, while the simulated ones are 8.52 dBi for LHCP and 7.21 dBi for RHCP, respectively.

The radiation patterns of the dual-CP antenna are measured at 13.5 GHz, which are plotted in Figure 18. It can be seen that the LHCP wave is co-polarization when port 1 is excited while the RHCP wave is co-polarization when port 2 is excited.

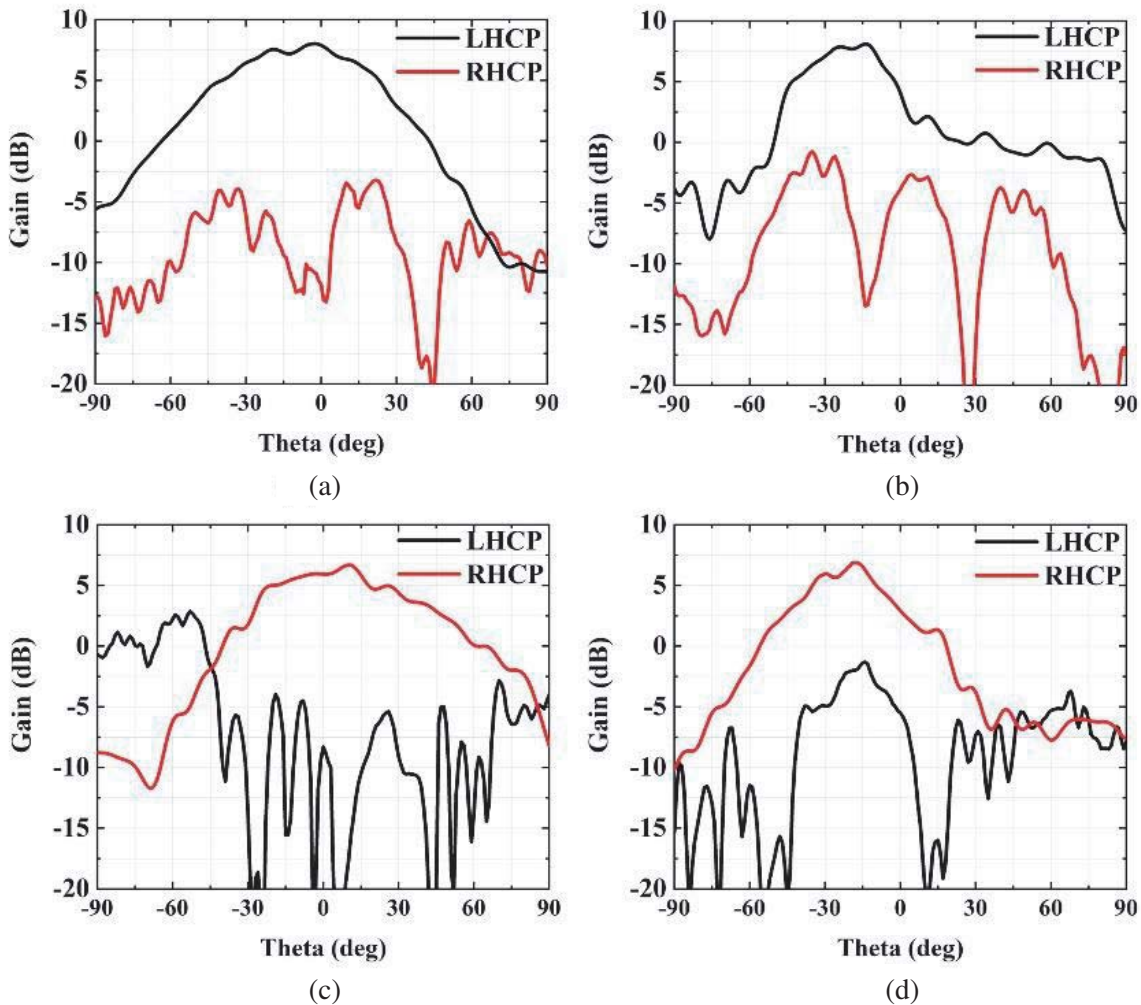


Figure 18. Measured radiation patterns of the designed dual-CP antenna at 13.5 GHz. (a) XOZ plane when port 1 is excited. (b) YOZ plane when port 1 is excited. (c) XOZ plane when port 2 is excited. (d) YOZ plane when port 2 is excited.

6. CONCLUSION

By placing a linearly-polarized printed bow-tie dipole above a reflective metasurface with cross-polarization conversion, the polarizations of the radiation waves above the dipole and the reflective waves are orthogonal. With an appropriate height between the printed dipole and metasurface, CP waves are generated. In this paper, the printed single bow-tie dipole and crossed dipole are applied

respectively, resulting in single-CP and dual-CP antennas. Good agreements between simulations and experiments are obtained. Experimental results demonstrate that the single-CP antenna achieves a 3-dB AR bandwidth of 8.0% (12.67–13.72 GHz) and a peak gain of 8.03 dBi while the dual-CP antenna has a bandwidth of 12.7% (12.67–14.39 GHz) and a peak gain of 8.49 dBi for LHCP and a bandwidth of 7.1% (13.09–14.05 GHz) and a peak gain of 7.03 dBi for RHCP. The isolation between the two ports of the dual-CP antenna is more than 20 dB. The proposed antenna can be applied to form an array, which can be a potential candidate for high-gain CP applications.

ACKNOWLEDGMENT

This work was supported by the National Natural Science Foundation of China (NSFC) (62071187), the Foreign Cooperation Projects of Quanzhou City Science and Technology Program of China (2017T006), and the Subsidized Projects for Postgraduates' Innovative Fund in Scientific Research of Huaqiao University (18013082025).

REFERENCES

1. Choi, E., J. W. Lee, and T. Lee, "Modified S-band satellite antenna with isoflux pattern and circularly polarized wide beamwidth," *IEEE Antennas Wireless Propag. Lett.*, Vol. 12, 1319–1322, 2013.
2. Gonzalez, I., J. Gomez, A. Tayebi, and F. Catedra, "Optimization of a dual-band helical antennas for TTC applications at S band," *IEEE Antennas Propag. Mag.*, Vol. 54, No. 4, 63–77, Aug. 2012.
3. Wu, Z., L. Li, Y. Li, and X. Chen, "Metasurface superstrate antenna with wideband circular polarization for satellite communication application," *IEEE Antennas Wireless Propag. Lett.*, Vol. 15, 374–377, 2016.
4. Chung, K. L., "High-performance circularly polarized antenna array using metamaterial-line based feed network," *IEEE Trans. Antennas and Propag.*, Vol. 61, No. 12, 6233–6237, Dec. 2013.
5. Deng, C., Y. Li, Z. Zhang, and Z. Feng, "A wideband sequential-phase fed circularly polarized patch array," *IEEE Trans. Antennas Propag.*, Vol. 62, No. 7, 3890–3893, Jul. 2014.
6. SalarRahimi, M., V. Volski, and G. A. E. Vandenbosch, "Mutual coupling-based compact wideband circularly polarized antenna," *IEEE Trans. Antennas Propag.*, Vol. 67, No. 7, 4872–4877, Jul. 2019.
7. Yang, S. L. S., K. F. Lee, and A. A. Kishk, "Design and study of wideband single feed circularly polarized microstrip antennas," *Progress In Electromagnetics Research*, Vol. 80, 45–61, 2008.
8. Yang, W., J. Zhou, Z. Yu, and L. Li, "Single-fed low profile broadband circularly polarized stacked patch antenna," *IEEE Trans. Antennas Propag.*, Vol. 62, No. 10, 5406–5410, Oct. 2014.
9. Abdulkarim, Y. I., L. W. Deng, J. L. Yang, Ş. Çolak, M. Karaaslan, S. X. Huang, L. H. He, and H. Luo, "Tunable left-hand characteristics in multi-nested square-split-ring enabled metamaterials," *J. Cent. South Univ.*, Vol. 27, 1235–1246, 2020.
10. Alkurt, F. O. and M. Karaaslan, "Pattern reconfigurable metasurface to improve characteristics of low profile antenna parameters," *Int. J. RF Microw. Comput. Aided. Eng.*, Vol. 29, e21790, 2019.
11. Yang, F. and Y. Rahmat-Samii, "A low profile single dipole antenna radiating circularly polarized waves," *IEEE Trans. Antennas Propag.*, Vol. 53, No. 9, 3083–3086, Sep. 2005.
12. Agarwal, K., Nasimuddin, and A. Alphones, "Wideband circularly polarized AMC reflector backed aperture antenna," *IEEE Trans. Antennas Propag.*, Vol. 61, No. 3, 1456–1461, Mar. 2013.
13. Nakamura, T. and T. Fukusako, "Broadband design of circularly polarized microstrip patch antenna using artificial ground," *IEEE Trans. Antennas Propag.*, Vol. 59, No. 6, 2103–2110, Jun. 2011.
14. Zhu, H. L., S. W. Cheung, K. L. Chung, and T. I. Yuk, "Linear-to-circular polarization conversion using metasurface," *IEEE Trans. Antennas Propag.*, Vol. 61, No. 9, 4615–4623, Sep. 2013.
15. Lin, C., Y. Ge, T. S. Bird, and K. Liu, "Circularly polarized horns based on standard horns and a metasurface polarizer," *IEEE Antennas Wireless Propag. Lett.*, Vol. 17, No. 3, 480–484, Mar. 2018.

16. Palma, L. D., A. Clemente, L. Dussopt, R. Sauleau, P. Potier, and P. Pouliguen, "Circularly polarized transmitarray with sequential rotation in Ka-band," *IEEE Trans. Antennas Propag.*, Vol. 63, No. 11, 5118–5124, Nov. 2015.
17. Liu, Y. and Y. Ge, "Polarization-reconfigurable flat transmitarray based on square frame and crossed dipole elements," *IEICE Trans. Commun.*, Vol. E100.B, No. 10, 1904–1910, Oct. 2017.
18. Chen, Y. Y., Y. Ge, and T. S. Bird, "An offset reflectarray antenna for multipolarization applications," *IEEE Antennas Wireless Propag. Lett.*, Vol. 15, 1353–1356, 2016.
19. Ta, S. X. and I. Park, "Low-profile broadband circularly polarized patch antenna using metasurface," *IEEE Trans. Antennas Propag.*, Vol. 63, No. 12, 5929–5934, Dec. 2015.
20. Ta, S. X. and I. Park, "Planar wideband circularly polarized metasurfacebased antenna array," *Journal of Electromagnetic Waves and Applications*, Vol. 30, No. 12, 1620–1630, 2016.
21. Lu, L., Y.-C. Jiao, W. Liang, and H. Zhang, "A novel low-profile dual circularly polarized dielectric resonator antenna," *IEEE Trans. Antennas Propag.*, Vol. 64, No. 9, 4078–4083, Sep. 2016.
22. Zheng, Y., M. Gao, and X. Zhao, "A novel patch array antenna with wideband and dual sense circular polarization characteristics for WiMAX & WLAN applications," *Progress In Electromagnetics Research C*, Vol. 99, 123–132, 2020.
23. Ferreira, R., J. Joubert, and J. W. Odendaal, "A compact dual-circularly polarized cavity-backed ring-slot antenna," *IEEE Trans. Antennas Propag.*, Vol. 65, No. 1, 364–368, Jan. 2017.
24. Zhu, J., S. Liao, Y. Yang, S. Li, and Q. Xue, "60-GHz dual circularly polarized planar aperture antenna and array," *IEEE Trans. Antennas Propag.*, Vol. 66, No. 2, 1014–1019, Feb. 2018.
25. Yang, W., Q. Meng, W. Che, L. Gu, and Q. Xue, "Low-profile wideband dual-circularly polarized metasurface antenna array with large beamwidth," *IEEE Antennas Wireless Propag. Lett.*, Vol. 17, No. 9, 1613–1616, Sep. 2018.
26. Huang, R., Z. Wang, G. Li, C. Lin, Y. Ge, and J. Pu, "A metasurface-enabled wideband high-gain dual-circularly-polarized fabry-perot resonator antenna," *Microw. Opt. Technol. Lett.*, Vol. 62, No. 10, 3195–3202, 2020.
27. Mao, C., Y. Yang, X. He, J. Zheng, and T. Liu, "Design of high-gain dual-band dual-circular-polarised antenna using reflective metasurface," *Electron. Lett.*, Vol. 53, No. 22, 1448–1450, Oct. 2017.
28. Cui, Y. H., R. L. Li, and H. Z. Fu, "A broadband dual-polarized planar antenna for 2G/3G/LTE base stations," *IEEE Trans. Antennas and Propag.*, Vol. 62, No. 9, 4836–4840, 2014.
29. Awl, H. N., Y. I. Abdulkarim, L. Deng, M. Bakir, F. F. Muhammadsharif, M. Karaaslan, E. Unal, and H. Luo, "Bandwidth improvement in bow-tie microstrip antennas: The effect of substrate type and design dimensions," *Appl. Sci.*, Vol. 10, No. 2, 504, 2020.
30. Milligan, T. A., *Modern Antenna Design*, 2nd Edition, Wiley, Hoboken, 2005.
31. Yin, J. Y., X. Wan, Q. Zhang, and T. J. Cui, "Ultra wideband polarization-selective conversion of electromagnetic waves by metasurface under large-range incidence angles," *Sci. Rep.*, Vol. 5, 12476, 2015.